

Investigation of Magnetic Anisotropy in Cobalt Chromium (CoCr_{0.5}Fe_{1.5}O₄) Spinel Ferrite Thin Films

Safia Anjum¹ · Ayesha Salman¹ · M. Shahid Rafique² · R. Zia¹ · S. Riaz³ · Hina Iqbal¹

Received: 25 April 2015 / Accepted: 19 May 2015 / Published online: 24 June 2015
© Springer Science+Business Media New York 2015

Abstract This project is aimed to the fabrication of thin films of chromium-substituted cobalt ferrites (CoCr_{0.5}Fe_{1.5}O₄) by electron beam deposition technique. After deposition, the thin films are post annealed at 200, 300, 400, and 500 °C for 1 h. The structural properties of thin films are investigated by X-ray diffraction (XRD) and Raman spectroscopy which confirm the inverse cubic spinel structure. It is revealed that the films become more crystalline as annealing temperature is increased. The films showed smooth surface morphology with RMS roughness of <0.1 nm. The magnetic measurements revealed that the easy axis is aligned perpendicular to the film plane, whereas

hard axis is aligned parallel to film plane. The magnetization and coercivity increases with annealing temperature which is attributed to the large grain size. Band gap energy and optical constants (refractive index, extinction coefficient, and dielectric function) decreases and increases with temperature indicative of good quality of films.

Keywords Spinel ferrites · Anisotropy field · Surface morphology · Optical properties

1 Introduction

Spinel ferrite thin films are promising candidates for high-frequency applications due to their remarkable electrical and magnetic properties [1]. These are effectively utilized as magnetic core materials with low iron loss, opto-magnetic devices, vertical recording magnetic materials, and in surface magnetism study [2, 3]. Among the various spinel ferrite materials, cobalt ferrite (CoFe₂O₄) is well-known to possess excellent chemical stability, good electrical insulation, Curie temperature of 793 K, and high corrosion resistivity [4]. Also, it is a well-known hard magnetic material having high coercivity (5.40 kOe) and moderate saturation magnetization (about 80 emu/g) [5].

The structure of cobalt ferrite have inverse spinel with space group *Fd3m* which is based on an oxygen fcc sublattice in which Co²⁺ and Fe³⁺ cations equally occupy the octahedral B sites, while the tetrahedral A sites are occupied by the remaining Fe³⁺ cations. Moreover only, an eighth of the tetrahedral sites are occupied by the Fe³⁺ ions, and only half of the 16 octahedral sites are occupied randomly by four Co²⁺ and four Fe³⁺ ions. This large fraction of empty interstitial sites creates a very open structure that permits cation migration [6]. Addition of non-magnetic Cr³⁺ ions could

✉ Safia Anjum
safia_anjum@hotmail.com

Ayesha Salman
Ayesha.gemini@hotmail.com

M. Shahid Rafique
shahid_rafique@hotmail.com

R. Zia
rzia1960@gmail.com

S. Riaz
saira.cssp@yahoo.com

Hina Iqbal
hina.bhati@ymail.com

¹ Department of Physics, Lahore College for Women University, Lahore, Pakistan

² Department of Physics, University of Engineering and Technology, Lahore, Pakistan

³ Centre of Excellence for Solid State Physics, University of the Punjab, Lahore, Pakistan

produce sufficient changes in the structure of cobalt ferrite because of its strong B site preference. Since Cr^{3+} ($3 \mu\text{B}$) has a weaker magnetic moment than Fe^{3+} ($5 \mu\text{B}$), the partial replacement of Fe^{3+} by Cr^{3+} ion will cause a decrease in saturation magnetization and coercivity. [7–9].

The nano structured thin films of cobalt ferrite have gained more attraction in the applications of magneto-optical recording due to their large perpendicular magnetocrystalline anisotropy [10]. Thin films of spinel ferrites can be prepared by e-beam reactive evaporation [11], pulsed laser deposition (PLD) [12, 13], sol–gel method [14, 15], molecular beam epitaxy [16], chemical vapor deposition [17], RF magnetron sputtering [18, 19], dip coating process [20], and spray pyrolysis [21].

This paper is devoted to the fabrication of chromium substituted cobalt ferrite ($\text{CoCr}_{0.5}\text{Fe}_{1.7}\text{O}_4$) thin films on glass substrate employing electron beam evaporation technique. An attempt has been made to study the effect of post annealing temperature on the fabricated films. The X-ray diffraction (XRD), Raman spectroscopy, atomic force microscopy (AFM), vibrating sample magnetometer (VSM), UV–visible spectroscopy, and spectroscopic ellipsometry (SE) measurements were carried out to reveal the structural, surface morphological, magnetic, and optical properties, respectively.

2 Experimental Setup

The thin films of chromiumdoped cobalt ferrite ($\text{CoCr}_{0.5}\text{Fe}_{1.5}\text{O}_4$) are fabricated by employing electron beam evaporation technique from high vacuum coating unit (Edward Auto-500). A set of four films are deposited on

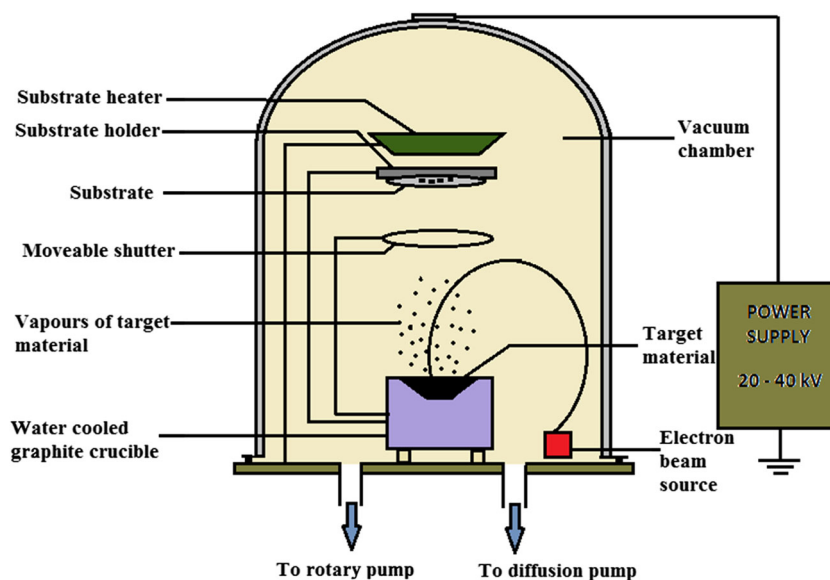
glass substrate keeping the substrate temperature constant at 100°C for all the thin films. The system is pumped down to a pressure of 1×10^{-4} torr. The target sample of $\text{CoCr}_{0.5}\text{Fe}_{1.5}\text{O}_4$ is sintered at temperature of 700°C for 1 h. Then the target is heated in the vacuum chamber with electron gun in order to degas the material before the evaporation process. An electron beam of sufficient intensity is emitted thermionically from filament (cathode) and focused on the target. The applied voltage is about 5 kV and beam current is 18 mA. The substrates are rotated during the deposition and the distance from the target pellets to the substrate is about 20 cm. The thickness of the films is about to be 250 nm. Film thicknesses and the rate of evaporation are monitored with a monitor attached to the vacuum system. The setup of electron beam apparatus is shown in Fig. 1. After deposition, the films are post annealed at temperature of 200, 300, 400 and 500°C for 1 h in the furnace. Then the films are cool down at room temperature inside the furnace.

3 Results and Discussion

3.1 XRD Analysis

The XRD micrographs of all the thin films, post annealed at different temperatures, are shown in Fig. 2. It can be seen from the figure that the film at 200°C annealing temperature does not show any peak revealing the amorphous nature of film. However, the diffraction peaks of (222), (400), and (440) start to appear for films annealed at 300, 400, and 500°C which confirm the face-centered cubic spinel structure. The peaks become narrower and sharper as the

Fig. 1 Experimental setup to grow thin films



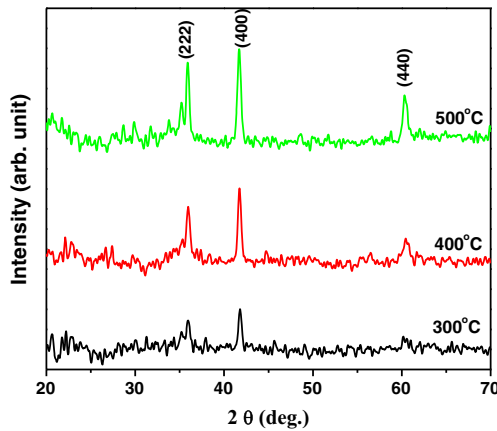


Fig. 2 XRD pattern of thin films annealed at 300, 400, and 500 °C

annealing temperature is increased. Since, the characteristic peak of ferrite is (311) which is absent in our XRD pattern, it could be due to the out of plane measurements of XRD (probably this peak lies in-plane of the film structure). It may also be possible that this peak has very small intensity as compared to other high intensity peaks appeared in pattern so that it gets merged with background noise [22].

The average crystallite size for the most intense peak of (400) is calculated by using Debye–Scherer’s formula [23]:

$$D = \frac{0.9\lambda}{\beta \cos \theta} \tag{3.1}$$

where D denotes the grain size, λ is the wavelength of the radiation ($CuK\alpha = 0.154 \text{ nm}$), β is the full width at half of the maximum intensity (radians), and θ is the Bragg angle. The estimated values of crystallite size are given in Table 1. The crystallite size increases with annealing temperature which corresponds to the coalescence of the grains due to the sufficient energy provided by the post annealing for proper orientation of grains. As a result, the crystallinity of films is improved [24].

3.2 Raman Spectroscopy Analysis

The microstructural analysis of all post annealed thin films is analyzed by the Raman spectroscopy at room temperature in the backscattering geometry with wavenumber range

Table 1 Average crystallite size of thin films at different temperatures

Annealing temperature(°C)	2θ (°)	Crystallite size (nm)
200	–	–
300	41.79	20.97
400	41.74	20.98
500	41.7	21.25

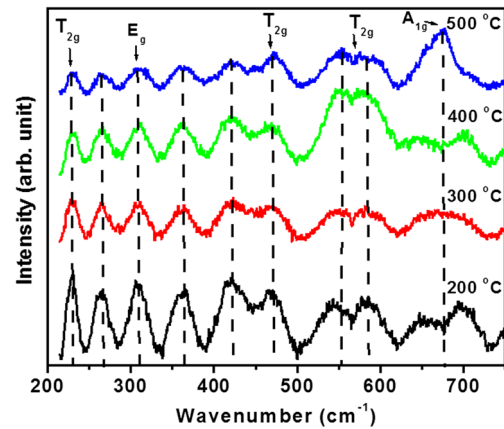


Fig. 3 Raman band positions of all post annealed thin films

200 to 750 cm^{-1} . Since, cobalt ferrite has inverted spinel structure which corresponds to space group (no. 227) and prototype symmetry O_h^7 . According to group theory, the vibrational modes of spinel structure are given by [25]

$$A_{1g}(R) + E_g(R) + T_{1g} + 3T_{2g}(R) + 2A_{2u} + 2E_{2u} + 4T_{1u}(IR) + 2T_{2u}$$

where R represents the Raman active modes and IR shows the infrared vibrational modes. For cubic spinel, five Raman active modes ($A_{1g} + E_g + 3T_{2g}$) are observed. The Raman spectra of all thin films are displayed in Fig. 3: The Raman active peaks appearing at 230, 309, 471, 567, and 696 cm^{-1} are characteristic modes of cobalt ferrite. It is observed from the standard library of Raman spectroscopy that the peaks in the region of 640–720 cm^{-1} indicates the modes of tetrahedral group and of A_{1g} type, while the peaks in the region of 400–620 cm^{-1} represent the modes assigned to octahedral group. The films at 200 to 400 °C annealing temperature, the band above 600 cm^{-1} have broad feature with a shoulder at $\sim 649 \text{ cm}^{-1}$ which becomes sharp at 500 °C indicates the fine structure of the film [26]. The T_{2g} mode exists below 600 cm^{-1} split in to two bands (at ~ 551 and $\sim 585 \text{ cm}^{-1}$) divulge the presence of two modes that have very close vibrational frequencies [27]. The peak intensities present at 266, 362, and 423 cm^{-1} are additional peaks which relates to the short range-ordering or non-equivalent atoms of the octahedral site [28]. The information of Raman peaks and assigned modes are listed in Table 2.

3.3 AFM Analysis

The surface morphology of all the thin films annealed at different temperatures is analyzed by AFM with scan area of $2 \mu\text{m} \times 2 \mu\text{m}$. The 2D and 3D images along with Y average filters are represented in Fig. 4. It is shown from the figure

Table 2 Raman modes of $\text{CoCr}_{0.5}\text{Fe}_{1.5}\text{O}_4$ thin films

Assigned modes	Raman modes (cm^{-1}) of thin films annealed at different temperatures			
	200	300	400	500
$T_{2g}(1)$	230	230	230	230
E_g	309	310	310	310
$T_{2g}(2)$	469	469	471	472
$T_{2g}(3)$	544	549	551	551
	585	585	583	583
A_{1g}	696	673	699	675

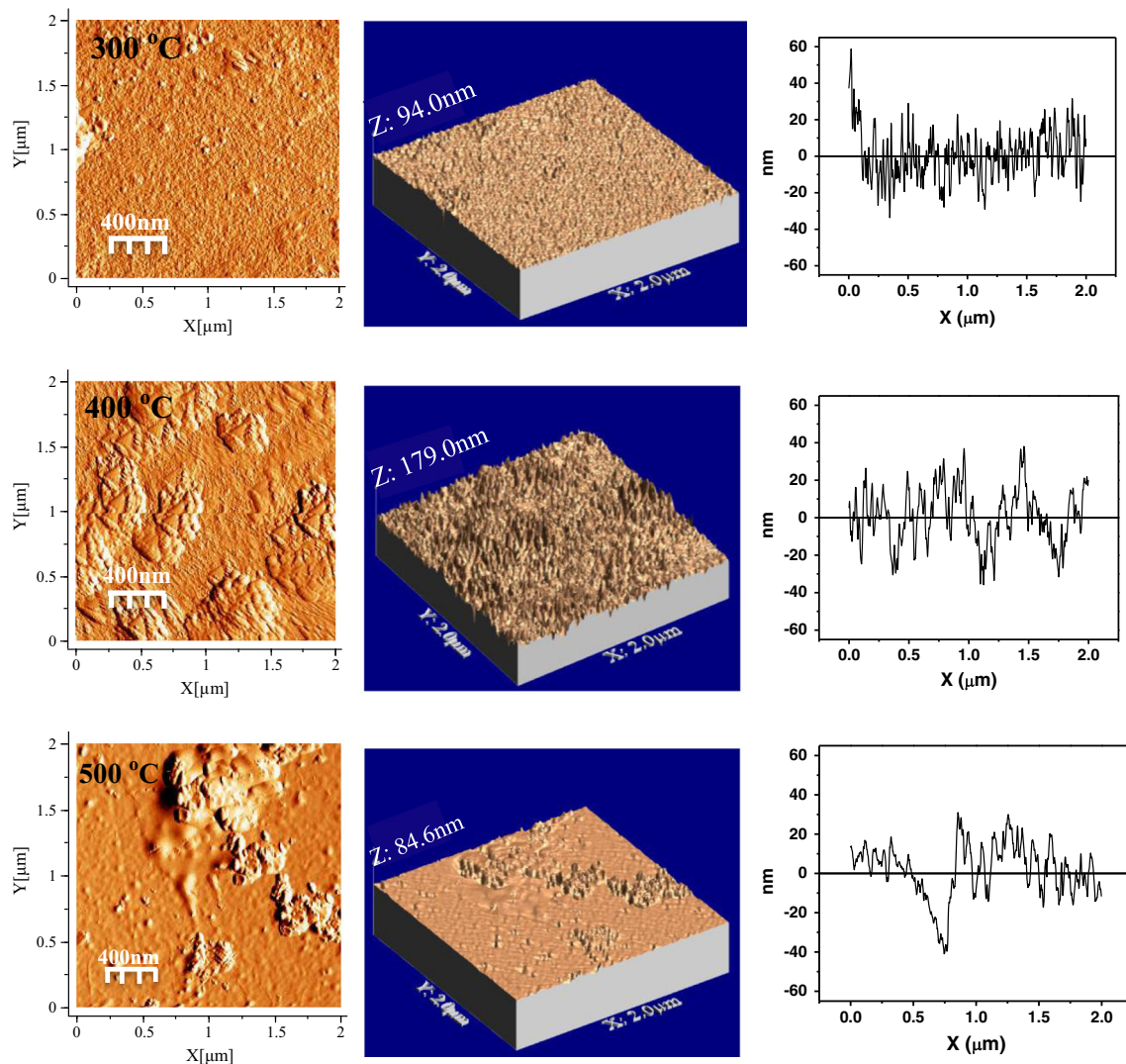
that all the films have smooth surface morphology with uniform distribution of particles. Also, the films exhibit the agglomeration of particles with a rise in annealing temperature. The Y average filter of thin films indicate the more

Table 3 Annealing dependent RMS roughness and roughness average for thin films

Annealing temperature ($^{\circ}\text{C}$)	RMS roughness (nm)	Roughness average (nm)
200	0.09	0.07
300	0.14	0.11
400	0.09	0.07
500	0.08	0.05

amplitude variation from the origin as the annealing temperature is increased which corresponds to the large particle size that reduced the grain boundaries, and therefore, RMS roughness is decreased [29]. The values of RMS roughness and roughness average are described in Table 3.

Both the RMS roughness and roughness average decreases as annealing temperature is increased. Though,

**Fig. 4** AFM images a 2D, b 3D view, and c Y average filter of thin films

the film annealed at 300 °C shows the greater RMS roughness of about 0.14 nm as shown in Fig. 5.

3.4 VSM Analysis

The magnetic behavior of thin films with different annealing conditions is studied by vibrating sample magnetometer (VSM). The parallel and perpendicular $M - H$ loops of all the thin films, measured at room temperature in the applied field of range 10 to -10 kOe, are shown in Fig. 6. It can be seen from the figure that the films indicate the easy axis is oriented in perpendicular to film structure, while hard axis is oriented in the parallel direction. All the films exhibit the uniaxial magnetic anisotropy in perpendicular direction. The magnetic anisotropy field H_A is deduced by extrapolating the parallel and perpendicular loop. The point where both loops intersect each other, draw a perpendicular to the x -axis. The value of x -axis gives the value of anisotropy field.

The values of saturation magnetization (M_s) increase as the post annealing temperature is raised from 200 to 500 °C. It is worth noted that the M_s just describes the maximum magnetization of the film but not the actual M_s . Although, the value of magnetization is lower than bulk value of cobalt ferrites (i.e., 425 emu/cc). It may be due to the presence of non-magnetic Cr^{+3} ions on the octahedral B site [30]. It may also be attributed to the larger grain size of the thin films as observed by XRD and AFM analysis [31].

The cation distribution of ferrites may affect the magnetic properties of films. It is illustrated by the exchange interaction mechanism of metal ion occurring between A and B sublattices. The net magnetic moment per formula unit of thin films is calculated by Neel’s model of ferrimagnetism.

$$n_B^N = M_B(X) - M_A(X) \tag{3.2}$$

where M_A and M_B are magnetic moments of A and B sublattices, respectively.

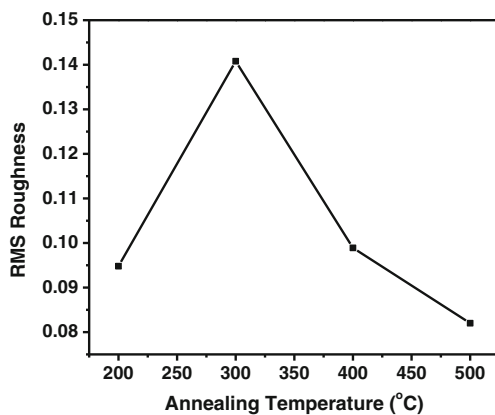


Fig. 5 RMS roughness of thin films as a function of annealing temperature

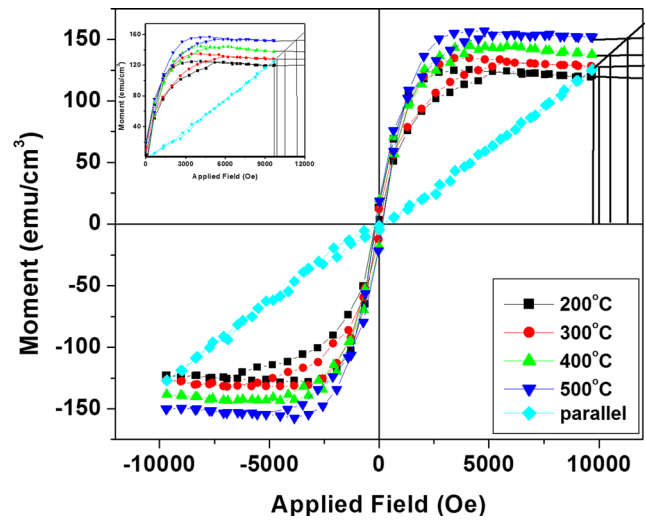


Fig. 6 Parallel and perpendicular $M-H$ hysteresis curve of $CoCr_{0.5}Fe_2O_4$ thin films annealed at different temperatures

In our case, the cation distribution suggests that both cobalt and chromium ions occupy the octahedral B sites. Due to annealing temperature, cation that migrates from one site to another causes the increase in exchange interaction. As a result, an increase in saturation magnetization occurs [23]. The H_c , M_r , and squareness also increase with annealing temperature. The derived magnetic parameters like M_s , H_c , M_r , H_A , and squareness of thin films at different annealing conditions are discussed in Table 4.

3.5 UV-Vis Spectroscopy Measurements

The optical properties of thin films, annealed at different temperatures, have been studied using UV-visible spectroscopy in the wavelength range of 200–600 nm. The absorption spectra of thin films, deposited on glass substrates, have been measured by placing uncoated identical glass substrate in reference beam. The UV-Vis absorbance spectra for all the thin films is shown in Fig. 7 which revealed the high absorbance in UV region, and this absorbance tend to decrease in visible region and near IR region [32].

The absorption coefficient, α , has been calculated from the following fundamental formulas [33]:

$$I = I_0 e^{-\alpha t}, A = \log \left(\frac{I_0}{I} \right)$$

$$\alpha = 2.303(Abs/t) \tag{3.3}$$

where t is the thickness of the film and Abs is the absorbance.

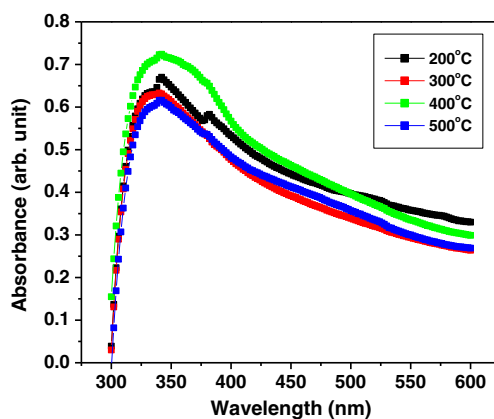
The optical band gaps for all the films have been calculated using the Tauc’s relation [34]:

$$(\alpha h\nu)^n = A(h\nu - E_g) \tag{3.4}$$

Table 4 Magnetic parameters of annealing dependent thin films

Annealing temperature (°C)	Magnetization M (emu/cc)	Coercivity H_c (Oe)	Retentivity M_r (emu/cc)	Squareness $R = M_r/M$	Anisotropic field H_A (kOe)
200	119.72	99.89	9.24	0.07	9.7
300	125.94	114.12	11.52	0.09	10
400	133.39	170.23	18.71	0.11	10.5
500	144.57	151.20	16.23	0.12	11.3

where $h\nu$ is photon energy, A is the constant, and n is an index that defines the optical absorption process and is theoretically equal to $n = 2$ for direct and $n = 1/2$ for indirect band gap. The band gap energy value have been deduced by plotting $h\nu$ vs. $(\alpha h\nu)^2$. The linear extrapolation at energy axis gives the value of the band gap energy. The linear shape of graph confirms the direct band gap nature of the thin films as shown in Fig. 8. The values of optical band gap of the thin films annealed at different temperatures are listed in Table 5. The results show that optical band gap decreases from 2.68 to 2.58 eV with the rise of annealing temperature from 200 to 500 °C. The decrease in band gap energy with increasing annealing temperature is caused by presence of an amorphous phase in thin films which is reduced by high annealing temperatures. Since more energy is required for crystalline growth, thus, high quality of thin films which causes reduction of the defect sites and interatomic spacing. This results are in consistent with the XRD results [35]. It can also be explained by two processes, cation ordering and oxidation deficiency, that occurs during the post annealing of thin films. The cation ordering process occurs instantly and forms the better inverse spinel structure favored by $\text{CoCr}_{0.5}\text{Fe}_{1.5}\text{O}_4$. While due to the oxygen deficiency (i.e., a long-range self-diffusion process), the vacancy annihilation process produces an ordered stoichiometric film [36].

**Fig. 7** UV-Vis spectra for all thin films at different temperatures

3.6 Spectroscopic Ellipsometry Measurements

Optical properties like band gap energy (E_g), refractive index (n), extinction coefficient (k), and dielectric constants (ϵ_1, ϵ_2) of thin films have been measured by spectroscopic ellipsometry (SE) at 300- to 1000-nm wavelength range. The ellipsometric data is investigated by employing Lorentz oscillator model.

The reflectance of all the film is measured from Beer's formula [34]:

$$R = \frac{(1 - n)^2 + k^2}{(1 + n)^2 + k^2} \quad (3.5)$$

where n and k are refractive index and extinction coefficients, respectively.

The reflectance spectra, shown in Fig. 9a, represent the enormous increase in reflectance for all the films at higher wavelengths. The maximum reflectance is observed in the range of 700–800 nm for the film annealed at 500 °C. After 800 nm, the reflectance starts to decrease in the IR region.

The transmittance spectra of all the films are demonstrated in Fig. 9b. This spectrum is a very important tool that exhibits the optical performance of the films. All the films revealed high transparency in the visible region which continues to increase in the IR region. The transmittance decreases with annealing temperature, which means that the films become more absorbable at high temperatures.

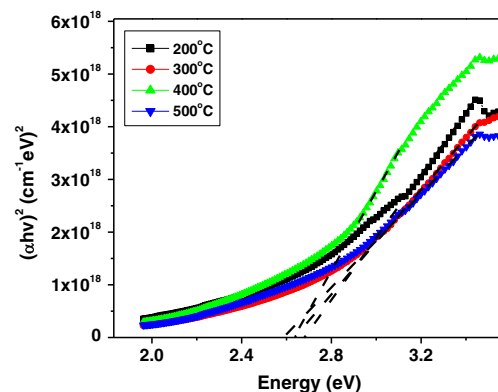
**Fig. 8** Band energy of $\text{CoCr}_{0.5}\text{Fe}_{1.5}\text{O}_4$ thin films post annealed at different temperature

Table 5 Band gap energies of films at different annealing temperatures

Annealing temperature (°C)	Band gap energy (eV)
200	2.68
300	2.63
400	2.63
500	2.58

The films exhibit better crystallinity due to which scattering phenomenon decreases [37].

The refractive index and dielectric constants define characteristics of optical materials and has significant role in designing devices for optical communication [25]. The refractive index and dielectric function of thin films are calculated according to following equations [34]:

$$n^* = n + ik \tag{3.6}$$

where real part is known as refractive index n . k is the imaginary part known as extinction coefficient.

$$\epsilon^* = \epsilon_1 - i\epsilon_2 \tag{3.7}$$

In this equation, the ϵ_1 and ϵ_2 are the real and imaginary dielectric constants, respectively. The real part of dielectric function is given by

$$\epsilon_1 = n^2 - k^2 \tag{3.8}$$

while imaginary part is equal to

$$\epsilon_2 = 2nk \tag{3.9}$$

The refractive index (n) of all the thin films annealed at different temperatures is depicted in Fig. 10a. It is observed from the figure that refractive index is high in the UV region and drops progressively in visible and IR region. At the wavelength of 400 nm, the value of n gradually increases from 1.92 to 2.04 as the annealing temperature is increased from 200 to 500 °C. This increasing trend of refractive

index with annealing temperature is attributed to improvement in quality of thin film due to which porosity in thin films decreases [38].

The variation of extinction coefficient with wavelength at different annealing temperatures, shown in Fig. 10b, revealed the similar behavior as that of refractive index, i.e., the extinction coefficient slightly increases with increase in annealing temperature. The maximum value of k , at 400 nm, is 0.29 at annealing temperature of 500 °C. The dependence of real and imaginary dielectric constants as a function of wavelength is illustrated in Fig. 11. Both real and imaginary dielectric constants depict the same trend as that of refractive index and extinction coefficient because of their dependence. Both ϵ_1 and ϵ_2 increases with increase in annealing temperature. Maximum values of $\epsilon_1 = 4.09$ and $\epsilon_2 = 1.17$ is observed for films annealed at 500 °C.

The values of optical parameters, i.e., refractive index, extinction coefficients, and dielectric function for all thin films annealed at different temperatures, are listed in Table 6.

The values of absorption coefficient (α) for all the thin films are calculated by using the following relation [39]:

$$\alpha = \frac{4\pi k}{\lambda} \tag{3.10}$$

The plot of α as a function of energy (eV) is displayed in Fig. 12a. The absorption coefficient for all thin films progressively increases with increasing energy (from 1.24 to 4.12 eV) until the energy reaches the value of approximately 4.12 eV. With the rise of annealing temperature, the absorption coefficient slightly increases at corresponding energy value.

The band gap energy for all thin films is calculated by Tauc’s relation:

$$\alpha h\nu = (h\nu - E_g)^n \tag{3.11}$$

where n is an index and $n = 1/2$ for direct band gap and $n = 2$ for indirect band gap. The plot of $(\alpha\nu)^2$ as a function of energy gives the direct band gap transition. The linear

Fig. 9 a Reflectance and b transmittance spectra of thin films annealed at different temperatures

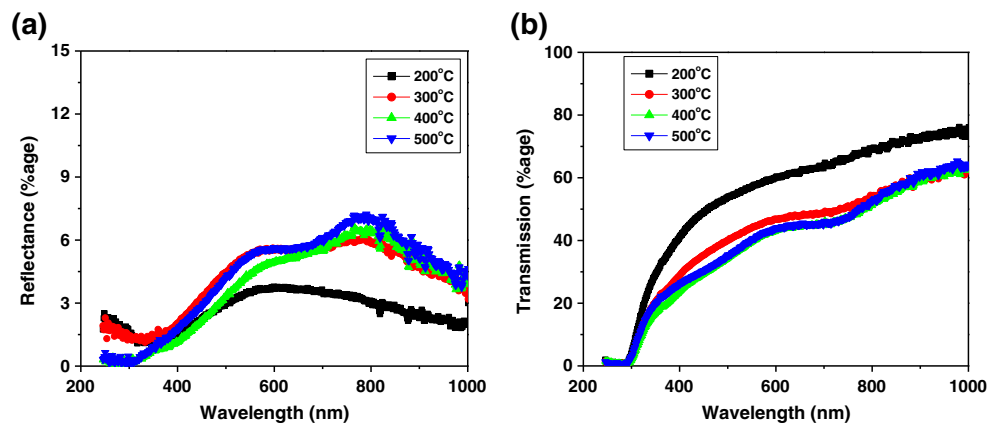


Fig. 10 **a** Refractive index and **b** extinction coefficient of thin films annealed at different temperatures

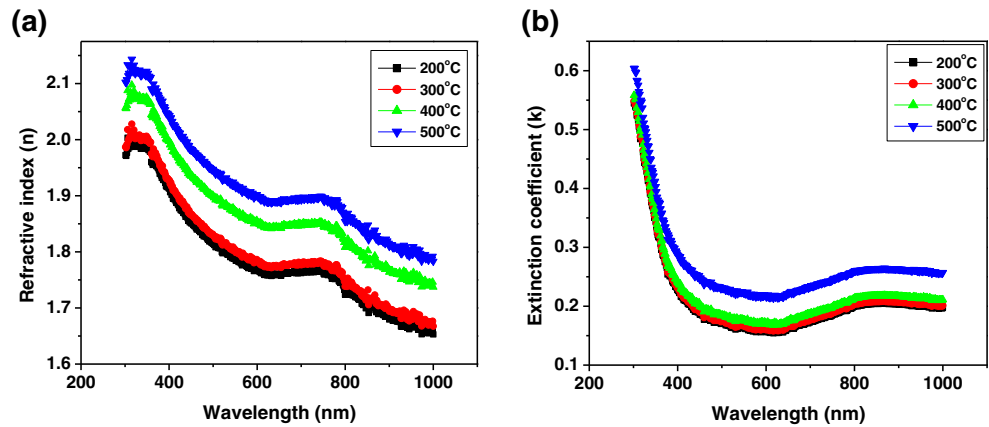


Fig. 11 **a** Real and **b** imaginary dielectric constants for all the thin films

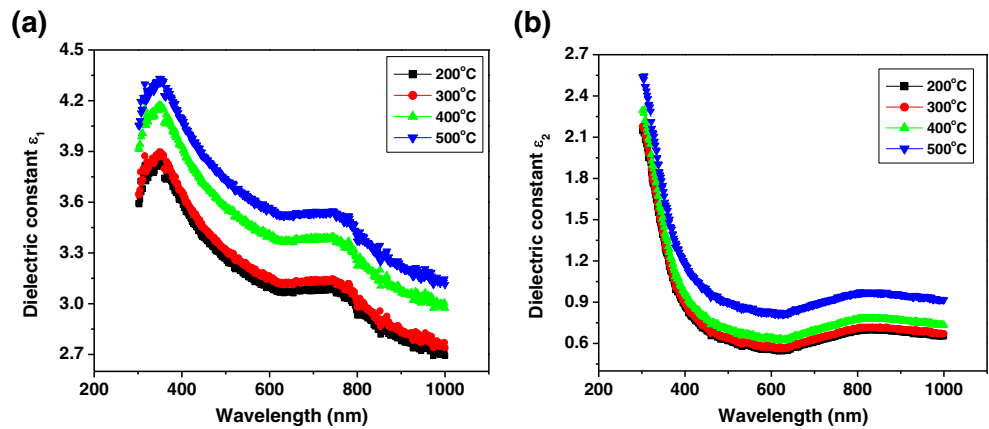


Table 6 Optical parameters of $C_0Cr_{0.5}Fe_2O_4$ thin films annealed at different temperatures at $\lambda=400$ nm

Annealing temperature °C	Reflectance %	Transmittance %	Refractive index n	Extinction coefficient k	Dielectric function		Absorption coefficient $\alpha \times 10^4$ (cm ⁻¹)
					ϵ_1	ϵ_2	
200	1.5	42	1.92	0.23	3.59	0.85	2.5
300	2.0	29	1.93	0.23	3.66	0.87	2.5
400	1.1	24	1.99	0.24	3.93	0.95	2.6
500	1.7	26	2.04	0.29	4.09	1.17	3.3

Fig. 12 **a** Absorption coefficient and **b** band gap energy as a function of energy (eV) of thin films annealed at different temperatures

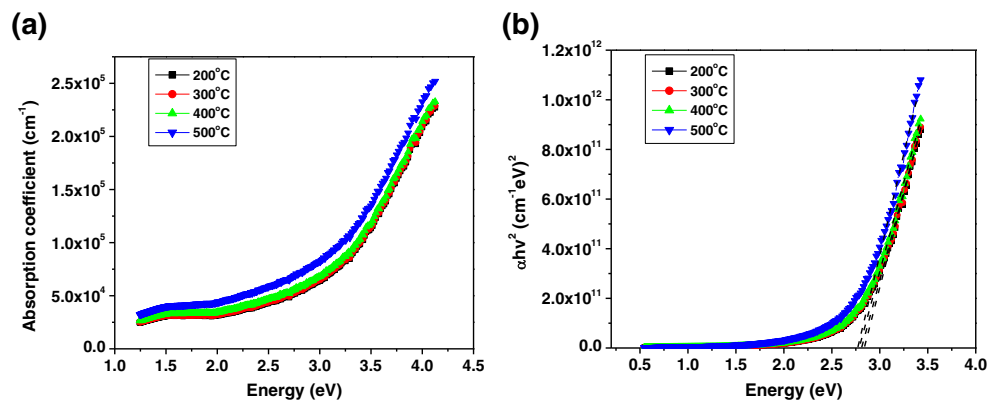


Table 7 Comparison of band gap energy values obtained by UV-visible Spectroscopy and Spectroscopic Ellipsometry analysis

Annealing temperature °C	Band gap energy (UVvisible)(eV)	Band gap energy (Ellipsometry)(eV)	Band gap shift
200	2.68	2.85	0.17
300	2.63	2.80	0.17
400	2.63	2.78	0.15
500	2.58	2.77	0.19

extrapolation on energy axis gives the value of band gap energy.

The band gap energies of thin films annealed at different temperatures are exhibited in Fig. 12b. It is evaluated from the figure that band gap decreases slightly from 3.56 to 3.51 eV as the annealing temperature is increased. The band gap energy is affected by several factors such as crystallite size, film thickness, carrier concentrations, lattice strain, and presence of impurities [40].

The variation of band gap energy with annealing temperature is shown in Fig. 12b. This behavior of band gap is because high annealing temperature is responsible for better quality of thin films as a result of which defect sites and porosity are reduced and interatomic spacing decreases [35]. However, cation ordering and oxygen deficiency are two main processes that take place during post annealing and make the inverse spinel structure and ordered stoichiometric films, respectively [36]. Thus, the results obtained from ellipsometry analysis are compatible with UV-Vis spectroscopy results. A comparison between band gap energies calculated from UV-Vis spectrophotometer and spectroscopic ellipsometry are given in Table 7.

As it can be seen from the table that the values of band gap energy evaluated from UV-Vis spectrophotometer is close to bulk values of CoFe_2O_4 . The inconsistency in values of band gap energies, obtained from both techniques, is because of the fact that the data of ellipsometry is based on models for data fitting between theoretical and experimental

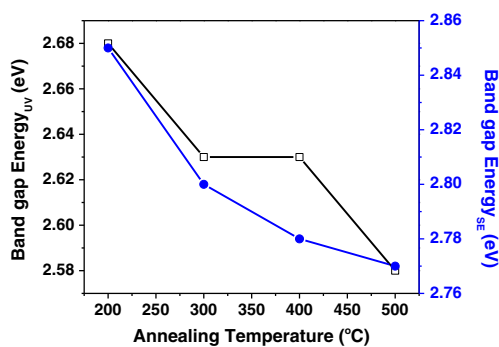
data [41]. The comparative graph of band gap energy calculated from both techniques is represented in Fig. 13.

4 Conclusions

Thin films of chromium-doped cobalt ferrites ($\text{CoCr}_{0.5}\text{Fe}_{1.5}\text{O}_4$) are grown employing electron beam evaporation technique. The structural, surface morphological, magnetic, and optical properties of thin films are studied under different post annealing temperatures. Thin film, annealed at 500 °C exhibits the better crystallinity due to increase in crystallite size as calculated by XRD data. The AFM images represents that the film have less RMS roughness (i.e., <0.1 nm) at 500 °C. The easy axis is oriented out-of-plane of the film structure, while hard axis is aligned in-plane of film. Both the magnetization and coercivity divulge the increasing trend with annealing temperature because of reduced defects and less grain boundaries. The optical constants like refractive index, extinction coefficient, and dielectric function (both real and imaginary) increase, while the value of band gap energy decreases as the annealing temperature is increased which corresponds to the better crystallinity of films. The comparison of band gap energy calculated from UV-Vis spectrophotometer and spectroscopy ellipsometry (SE) showed the minute difference in band gap values which corresponds to the difference in data analysis.

References

- Venzke, S., van Dover, R.B., Philips, J.M., Gyorgy, E.M., Siegrist, T., Chen, C.H., Werder, D., Fleming, R.M., Felder, R.J., Coleman, E., Opila, R.: Epitaxial growth and magnetic behavior of NiFe_2O_4 thin films. *J. Mater. Res.* **11**(5) (1996)
- Alvarado, S.F.: Magnetism of surfaces by spin polarized photoemission. *Z. Phys. B* **33**, 51 (1979)
- Shinjo, T., Kiyama, M., Sugita, N., Watanabe, K., Takada, T.: Surface magnetism of $\alpha\text{-Fe}_2\text{O}_3$ by Mossbauer spectroscopy. *J. Magn. Magn. Mater.* **35**, 133–135 (1983)
- Lisfi, A., Williams, C.M., Nguyen, L.T., Ladder, J.C., Coleman, A., Corcoran, H., Johnson, A., Chang, P., Kumar, A., Morgan, W.: Investigation of magnetic anisotropy in epitaxial cobalt ferrite thin films. *Phys. Rev. B* **76**, 054405 (2007)
- Maheshkumar L. M., Dhage, V.N., Sundar, R., Ranganathan, K., Oak, S.M., Shengule, D.R., Jadhav, K.M.: Effects of Nd:YAG laser irradiation on structural, morphological, cation distribution and magnetic properties of nanocrystalline CoFe_2O_4 . *Appl. Surf. Sci.* **257**, 8511–8517 (2011)
- Lüders, U., Bibes, M., Bouzehouane, K., Jacquet, E., Contour, J.-P., Fusil, S., Bobo, J.-F., Fontcuberta, J., Barthélémy, A., Fert, A.: Spin filtering through ferrimagnetic NiFe_2O_4 tunnel. Barriers *Appl. Phys. Lett.* **88**, 082505 (2006)
- Birajdar, A.A., Shirsath, S.E., Kadam, R.H., Patange, S.M., Mane, D.R., Shitre, A.R.: Frequency and temperature dependent electrical properties of $\text{Ni}_{0.7}\text{Zn}_{0.3}\text{Cr}_x\text{Fe}_{2-x}\text{O}_4$ ($0 \leq x \leq 0.5$). *Ceram. Int.* **38**, 2963–2970 (2012)

**Fig. 13** Comparative graph of band gap energy vs. annealing temperature

8. Sankpal, A.M., Suryavanshi, S.S., Kakatkar, S.V., Tengshe, G.G., Patil, R.S., Chaudhari, N.D., Sawant, S.R.: Magnetization studies on aluminum and chromium substituted Ni–Zn ferrites. *J. Magn. Mater.* **186**, 349 (1998)
9. Lakshman, A., Rao, K.H., Mendiratta, R.G.: Magnetic properties of In^{3+} and Cr^{3+} substituted Mg–Mn ferrites. *J. Magn. Mater.* **250**, 92 (2002)
10. Zhang, H.Y., Gu, B.X., Zhai, H.R., Lu, M., Huang, H.B.: Magneto-optical properties and anisotropy of cobalt ferrite films with different texture. *J. Magn. Mater.* **140–144**, 699–700 (1995)
11. Kado, T.: Epitaxial composites of Sr ferrite and hematite grown on Al_2O_3 by electron beam deposition and heat treatment. *Br. J. Appl. Phys.* **100**, 053906 (2006)
12. Chinta, P.V., Callori, S.J., Dawber, M., Ashrafi, A., Headrick, R.L.: Transition from laminar to three-dimensional growth mode in pulsed laser deposited BiFeO_3 film on (001) SrTiO_3 . *Appl. Phys. Lett.* **101**, 201602 (2012)
13. Chen, Y.C., Wang, G.F., Tai, H.H., Chen, J.W., Huang, Y.C., Yang, J.C., Chu, Y.H.: Non-volatile domain nucleation and growth in multiferroic BiFeO_3 films. *Nanotechnology* **22**, 254030 (2011)
14. Chen, B., Li, M., Liu, Y.W., Zuo, Z.H., Zhuge, F., Zhan, Q.F., Li, R.W.: Effect of top electrodes on photovoltaic properties of polycrystalline BiFeO_3 based thin film capacitors. *Nanotechnology* **22**, 195201 (2011)
15. Zhang, D.H., Shi, P., Wu, X.Q., Ren, W.: Structural and electrical properties of sol–gel-derived Al-doped bismuth ferrite thin films. *Ceram. Int.* **39**, 461–464 (2013)
16. Ihlefeld, J.F., Podraza, N.J., Liu, Z.K., CRai, R., Xu, X., Heeg, T., Chen, Y.B., Li, J., Collins, R.W., Musfeldt, J.L., Pan, X.Q., Schubert, J., Ramesh, R., Schlom, D.G.: Optical band gap of BiFeO_3 grown by molecular-beam epitaxy. *Appl. Phys. Lett.* **92**, 142908 (2008)
17. Zhang, J.X., Xiang, B., He, Q., Seidel, J., Zeches, R.J., Yu, P., Yang, S.Y., Wang, C.H., Chu, Y.H., Martin, L.W., Minor, A.M., Ramesh, R.: Large field-induced strains in a lead-free piezoelectric material. *Nat. Nanotechnol.* **6**, 98–102 (2011)
18. Lee, H.J., Park, M.H., Kim, Y.J., Hwang, C.S., Kim, J.H., Funakubo, H., Ishiwara, H.: Improved ferroelectric property of very thin Mn-doped BiFeO_3 films by an inlaid Al_2O_3 tunnel switch. *Br. J. Appl. Phys.* **110**, 074111 (2011)
19. Fan, F., Luo, B.C., Duan, M.M., Xing, H., Jin, K.X., Chen, C.L.: Ferro-electric domain switching investigation of BiFeO_3 thin film on Pt/Ti/SiO₂/Si (111) substrate. *Appl. Surf. Sci.* **258**, 7412–7416 (2012)
20. Tsuchiya, T., Yamashirao, H., Sci, T., Inamura, T.: Preparation of spinel-type ferrite thin films by the dip-coating process and their magnetic properties. *Asian J. Mater. Sci.* **27**, 3645 (1992)
21. Chung, Y., Park, S., Kang, D.: Magnetically separable titania-coated nickel ferrite photocatalyst. *Mater. Chem. Phys.* **86**, 375 (2004)
22. Raghavender, A.T., Hong, N.H., Park, C., Jung, M., Lee, K.J., Lee, D.: Effect of annealing conditions on structural and magnetic properties of laser ablated copper ferrite thin films. *J. Magn. Mater.* **324**, 1814–1817 (2012)
23. Koseoglu, Y., Olewi, M.I., Yilgin, R., Kocbay, A.N.: Effect of chromium addition on structural, morphological and magnetic properties of nano-crystalline cobalt ferrite system. *Ceram. Int.* **38**, 6671–6676 (2012)
24. Jauhar, S., Goyal, A., Lakshmi, N., Chandra, K., Singhal, S.: Doping effect of Cr^{3+} ions on the structural, magnetic and electrical properties of Co–Cd ferrites: a study on the redistribution of cations in $\text{CoCd}_{0.4}\text{Cr}_x\text{Fe}_{1.6-x}\text{O}_4$ ($0.1 \leq x \leq 0.6$) ferrites. *Mater. Chem. Phys.* **139**, 836–843 (2013)
25. Dixit, G., Singh, J.P., Srivastava, R.C., Agarwal, H.M., Choudhary, R.J.: Structural, magnetic and optical studies of nickel ferrite thin films. *Adv. Matt. Lett.* **3**(1), 21–28 (2012)
26. Thomasson, A., Kreisel, J., Lefevre, C., Roulland, F., Versini, G., Barre, S., Viart, N.: Raman scattering of magnetoelectric gallium ferrite thin films. *J. Phys. Condens. Matter* **25**(045401), 1–6 (2013)
27. Zhongwu, W., Schiferl, D., Zhao, Y., O'Neill, H.St.C.: High pressure Raman spectroscopy of spinel-type ferrite ZnFe_2O_4 . *J. Phys. Chem. Solids* **64**, 2517–2523 (2003)
28. Himcinschi, C., Vrejoiu, I., Salvan, G., Fronk, M., Talkenberger, A., Dietrich, R.T., Zahn, D.R., Kortus, J.: Optical and magneto-optical study of nickel and cobalt ferrite epitaxial thin films and submicron structures. *Journal Of Applied Physics* **113**, 084101 (2013)
29. SafiaAnjum (PHD thesis), Growth of nano-structured thin films of magnetic materials by PLD technique, 2011
30. Vasambekar, P.N., Kolekar, C.B., Vaingankar, A.S.: Magnetic behavior of Cd^{+2} and Cr^{+3} substituted cobalt ferrites. *Mater. Chem. Phys.* **60**, 282–285 (1999)
31. Chauhan, B.S., Kumar, R., Jadhav, K.M., Singh, M.: Magnetic study of substituted Mg–Mn ferrites synthesized by citrate precursor method. *J. Magn. Mater.* **283**, 71–81 (2004)
32. Bilecka, I., Kubli, M., amstad, E., Niederberger, M.: Simultaneous formation of ferrite nanocrystals and deposition of thin films via microwave-assisted non-aqueous sol-gel process. *J. Sol-Gel Sci. Technol.* **57**, 313–322 (2011)
33. Singhal, S., Bhukal, S., Singh, J., Chandra, K., Bansal, S.: Optical x-ray diffraction and magnetic properties of the cobalt substituted nickel chromium ferrites synthesized using sol-gel autocombustion method. *J. Nanomater.*, 1–6 (2011)
34. Abdelmoneim, H.M.: Optical properties of $\text{Ti}_{0.5}\text{Li}_{0.5}\text{La}_{0.1}\text{Fe}_{1.9}\text{O}_4$ ferrite thin films. *Physica B journal* **405**, 1551–1557 (2010)
35. Bao, D.H., Yao, X., Wakiya, N., Shinozaki, K., Mizutani, N.: Band-gap energies of sol-gel-derived SrTiO_3 thin films. *Appl. Phys. Lett.* **79**(23), 3767–3772 (2001)
36. Axelsson, A.-K., Valant, M., Fenner, L., Wills, A.S., McN Alford, N.: Chemistry of post annealing of epitaxial CoFe_2O_4 thin films. *Thin Solid Films* **517**, 3742–3747 (2009)
37. Patil, V., Joshi, P., Chougule, M., Sen, S.: Synthesis and characterization of Co_3O_4 thin film. *Soft Nanoscience Letters* **2**, 1–7 (2012)
38. Moustaghfir, A., Tomasella, E., Ben Amor, S., Jacquet, M., Cellier, J., Sauvage, T.: Structural and optical studies of ZnO thin films deposited by r.f. magnetron sputtering: influence of annealing. *Surf. Coat. Technol.* **174–175**, 193–196
39. Safia Anjum, M.S., Rafique, M., Khaleeq-ur-Rahman, K., Siraj, A., Usman, H., Latif, K.A., Bhatti, S., Hussain, S.: Naseem, Magnetic and optical properties of amorphous NdFeCo thin films by pulsed laser deposition technique. *Vacuum* **85**, 126–130 (2010)
40. Chavan, S.M., Babrekar, M.K., More, S.S., Jadhav, K.M.: Structural and optical properties of nanocrystalline Ni–Zn ferrite thin films. *J. Alloys Compd.* **507**, 21–25 (2010)
41. Iqbal, A., Mahmood, A., Khan, T.M., Ahmed, E.: Structural and optical properties of Cr doped ZnO crystalline thin films deposited by reactive electron beam evaporation technique. *Prog. Nat. Sci.: Mater. Int.* **23**(1), 64–69 (2013)